OPEN ACCESS

University of BRISTOL

Khodr, C., Azarpeyvand, M., & Green, D. (2020). An iterative three-dimensional parabolic equation solver for propagation above irregular boundaries. *Journal of the Acoustical Society of America*, *148*(2), [1089 (2020)]. https://doi.org/10.1121/10.0001766

Publisher's PDF, also known as Version of record

Link to published version (if available):
10.1121/10.0001766

Link to publication record in Explore Bristol Research
PDF-document

This is the final published version of the article (version of record). It first appeared online via Acoustical Society of America at https://doi.org/10.1121/10.0001766. Please refer to any applicable terms of use of the publisher.

University of Bristol - Explore Bristol Research
General rights

This document is made available in accordance with publisher policies. Please cite only the published version using the reference above. Full terms of use are available:
http://www.bristol.ac.uk/red/research-policy/pure/user-guides/ebr-terms/

An iterative three-dimensional parabolic equation solver for propagation above irregular boundaries

Codor Khodr, Mahdi Azarpeyvand, and David N. Green

Citation: The Journal of the Acoustical Society of America **148**, 1089 (2020); doi: 10.1121/10.0001766
View online: https://doi.org/10.1121/10.0001766
View Table of Contents: https://asa.scitation.org/toc/jas/148/2
Published by the Acoustical Society of America

ARTICLES YOU MAY BE INTERESTED IN

Model-based Bayesian analysis in acoustics—A tutorial
The Journal of the Acoustical Society of America **148**, 1101 (2020); https://doi.org/10.1121/10.0001731

Machine learning in acoustics: Theory and applications
The Journal of the Acoustical Society of America **146**, 3590 (2019); https://doi.org/10.1121/1.5133944

Deconvolution of decomposed conventional beamforming
The Journal of the Acoustical Society of America **148**, EL195 (2020); https://doi.org/10.1121/10.0001764

A computational method whose time had come
The Journal of the Acoustical Society of America **148**, R7 (2020); https://doi.org/10.1121/10.0002055

Wave and extra-wide-angle parabolic equations for sound propagation in a moving atmosphere
The Journal of the Acoustical Society of America **147**, 3969 (2020); https://doi.org/10.1121/10.0001397

A coupled mode model for omnidirectional three-dimensional underwater sound propagation
The Journal of the Acoustical Society of America **148**, 51 (2020); https://doi.org/10.1121/10.0001517

JASA ARTICLE

An iterative three-dimensional parabolic equation solver for propagation above irregular boundaries

Codor Khodr,[1,a)] Mahdi Azarpeyvand,[1,b)] and David N. Green[2]
[1]*Mechanical Engineering, University of Bristol, Bristol BS8 1TR, United Kingdom*
[2]*AWE Blacknest, Brimpton RG7 4RS, United Kingdom*

ABSTRACT:
This paper describes the development of an iterative three-dimensional parabolic equation solver that takes into account the effects of irregular boundaries and refraction from a layered atmosphere. A terrain-following coordinate transformation, based on the well-known Beilis-Tappert mapping, is applied to the narrow-angle parabolic equation in an inhomogeneous media. The main advantage of this approach, which has been used in two dimensions in the past, is the simplification of the impedance boundary condition at the earth's surface. The transformed initial-boundary value problem is discretized using the Crank-Nicholson marching scheme in the propagating direction and second-order finite-differences in the transversal plane. The proposed method relies on an efficient iterative fixed-point solver, which involves the inversion of tridiagonal matrices only. The accuracy of the method is evaluated through a comparison with boundary element simulations in a homogeneous atmosphere above a Gaussian hill. Results show that transversal scattering occurs in the shadow zone of the obstacle where the two-dimensional parabolic equation underestimates the pressure amplitude. The model is particularly suited for the simulation of infrasound in a three-dimensional environment with realistic topographies. © *2020 Acoustical Society of America*.
https://doi.org/10.1121/10.0001766
(Received 19 February 2020; revised 29 July 2020; accepted 30 July 2020; published online 28 August 2020)
[Editor: Vladimir E. Ostashev] Pages: 1089–1100

I. INTRODUCTION

Among the many numerical methods for long-range wave propagation, the parabolic equation (PE) has been proven to be one of the most efficient and versatile. This approximation to the Helmholtz equation, governing the propagation of a harmonic wave of angular frequency $\omega = 2\pi f$, was first introduced by Leontovich (1944) in the context of electromagnetic propagation. It was then applied to underwater acoustics (Tappert, 1977) and atmospheric acoustics (West *et al.*, 1992; White, 1989) with very promising results. While initial formulations of the PE were constrained to two-dimensional (2D) space (Collins, 1989; Thomson and Chapman, 1983), later models harnessed better computational resources to model three-dimensional (3D) propagation (Lee *et al.*, 1992; Siegmann *et al.*, 1985; Sturm, 2005). Over the past decades, substantial efforts have been dedicated to the study of theoretical and numerical aspects of the PE, leading to an increased number of practical applications. Extensive literature reviews of existing PE models and case studies are available in Lee *et al.* (2000) and Xu *et al.* (2016).

Since the PE method is an initial-boundary value problem (IBVP), the treatment of the boundary condition at the ground surface is crucial to the accurate estimation of the scattered field. In atmospheric acoustics, the ground is usually modeled as a locally or extended reacting surface with an acoustic impedance that is extracted from porous ground models (Attenborough, 1985; Attenborough *et al.*, 2011). When the boundary is flat, the impedance boundary condition (IBC) is readily included in the numerical scheme. However, the presence of irregular terrain at the bottom edge makes the numerical solution of the PE more challenging to implement. A common solution is to use a boundary fitted coordinate transform to express the PE in a numerical domain with a flat ground. Such techniques have been extensively used in 2D: notable contributions include the Generalized Terrain PE (GTPE) (Sack and West, 1995) and the Beilis-Tappert PE (BTPE) (Parakkal *et al.*, 2012), which both rely on the Beilis and Tappert (1979) mapping. A similar approach has been used in conjunction with finite-elements by Kampanis *et al.* (2013) to model propagation over irregular terrain in a refractive atmosphere.

A recurring issue in atmospheric acoustics is the modeling of 3D effects from irregular terrain, which plays an important role in situations where out-of-plane propagation cannot be ignored. In particular, the inclusion of irregular boundaries in the 3D PE is an open problem that has no straightforward solution. In the past, a few authors have managed to include irregular boundaries in the 3D PE, including Silva *et al.* (2012), who extended the Beilis-Tappert method to model 3D electromagnetic propagation above irregular terrain and used a direct solver to compute the solution. More recently, Lin (2019) has introduced a slip-step boundary-fitted 3D PE, based on non-uniform Galerkin discretization, for the inclusion of irregular waveguides in the context of underwater sound propagation. In

[a)]Electronic mail: codor.kh@gmail.com, ORCID: 0000-0003-4059-8521.
[b)]ORCID: 0000-0001-7826-7635.

this paper, a 3D version of the Beilis-Tappert mapping is used to express the 3D PE in a shifted coordinate system with simplified boundary conditions at the ground surface.

Numerical solutions of 3D problems are significantly more challenging to derive and implement than for 2D problems. When the three-dimensional parabolic equation (3D PE) is solved through direct methods, either with finite-differences (Cheng *et al.*, 2009) or finite-elements (Sturm and Kampanis, 2007), the resulting linear system involves very large sparse matrices. Such linear systems are computationally intensive to solve and typically require the use of iterative methods, such as the Generalized Minimal Residual (GMRES) or the Bi-Conjugate Gradient (BiCG) (Saad, 2003). To avoid this difficulty, most 3D PE models rely on the Alternate Direction Implicit (ADI) numerical scheme, which involves a splitting of the square-root operator into two one-dimensional (1D) operators (Sturm, 2005; Lin *et al.*, 2012). In this paper, a different approach, based on matrix equations and involving tridiagonal matrices only, is used to solve the 3D PE in the transformed coordinate system. Such a method has been previously used in electromagnetic propagation by Zelley and Constantinou (1999), who showed its suitability for the inclusion of irregular terrain in 3D. It is here adapted to acoustic propagation in a refractive atmosphere.

The rest of the paper is organized as follows: the Beilis-Tappert coordinate transformation is applied to the narrow-angle 3D PE in a refractive atmosphere in Sec. II, the finite-difference discretization and iterative numerical scheme are presented in Sec. III, validation against the acoustic boundary element method (BEM) for a simple scattering case in a homogeneous atmosphere is provided in Sec. IV, conclusions and further suggestions are given in Sec. V.

II. MATHEMATICAL MODELING

Here we present the general theory behind the PE method in a 3D Cartesian space, described by the coordinate system, $\mathbf{x} = (x, y, z)$. This requires considering the inclusion of: a layered moving atmosphere (Sec. II A), the topography of the ground surface via a Bellis-Tappert coordinate transform (Sec. II B), the impedance boundary conditions at the ground surface (Sec. II C), and the Gaussian starter field (Sec. II D).

A. Parabolic equation in a layered moving atmosphere

In atmospheric acoustics, the atmosphere is generally assumed to be a layered medium, defined by a temperature $T(z)$, density $\rho(z)$, and wind velocity $\mathbf{v}(z) = (v_x, v_y, v_z)$. When sound propagates in a stratified motionless medium, the wavefront turns according to the gradient of the sound speed $c(z)$, following Snell's law. This effect is known as refraction and plays a major role in low-frequency propagation at long ranges. For an adiabatic atmosphere, the sound speed is given by

$$c(z) = \sqrt{\gamma R T(z)} = c_0 \sqrt{T(z)/T_0}, \tag{1}$$

where $\gamma = 1.4$ is the specific heat ratio of air, $R = 287$ J/(kg.K) is the perfect gas constant of dry air, T_0 is the temperature at the ground surface, and c_0 is the corresponding adiabatic sound speed. An important simplification of the atmospheric model can be achieved by the effective sound speed approximation, which includes the medium motion through an effective sound speed defined as $c_{\text{eff}}(z) \simeq c(z) + \mathbf{v}(z) \cdot \mathbf{s}$ where $\mathbf{s}$ is the unit vector tangential to the sound ray. Taking x to be the direction of propagation leads to

$$c_{\text{eff}}(z) = c(z) + v_x(z), \tag{2}$$

and the effective wavenumber is defined as $k_{\text{eff}} = \omega / c_{\text{eff}}$. While this assumption has limitations, extensively discussed in Godin (2002), it considerably simplifies the governing equations for an inhomogeneous moving medium.

In this context, Ostashev and Wilson (2016) provide the following narrow-angle PE for an inhomogeneous moving atmosphere;

$$\left\{ 2ik_0 \frac{\partial}{\partial x} + \Delta_\perp + \delta k_{\text{eff}}^2 + \frac{2ik_0}{c_0} \mathbf{v}_\perp \cdot \nabla_\perp \right\} \psi = 0, \tag{3}$$

where $\mathbf{v}_\perp$ is the transversal wind velocity, $\nabla_\perp$ is the transversal gradient, $\Delta_\perp = \nabla_\perp^2$ is the transversal Laplacian operator, $k_0 = \omega / c_0$ is the ambient acoustic wavenumber, and $\delta k_{\text{eff}}^2 = k_{\text{eff}}^2 - k_0^2$ is the effective wavenumber variation. In the corresponding reference, Eq. (3) is derived without using the effective sound speed approximation, and k_{eff} is here introduced to regroup refractive terms. In Eq. (3), ψ is the complex pressure envelope, defined as

$$\psi(\mathbf{x}, \omega) = p(\mathbf{x}, \omega) e^{-ik_0 x}. \tag{4}$$

The wave field ψ represents the part of the complex pressure p that varies slowly with the distance x. Equation (3) is valid as long as the wavelength is small compared to the characteristic length of the medium inhomogeneity. The last term in Eq. (3) represents advection from wind in the transversal directions and can be neglected for weak wind conditions, in which case Eq. (3) reduces to the standard narrow-angle PE, well known in the literature (Lee *et al.*, 1992; Tappert, 1977; Sturm, 2005). Density variation with altitude is taken into account by multiplying the complex pressure ψ by a factor $\sqrt{\rho(z)/\rho_0}$, where ρ_0 is the reference density, without loss of accuracy (Ostashev and Wilson, 2016). The PE given in Eq. (3) is well suited for atmospheric acoustics and is used here to model long range propagation over irregular terrain.

B. Beilis-Tappert coordinate transformation

A boundary-following coordinate transformation is applied to the narrow-angle PE, given in Eq. (3), in order to transform the physical domain, with an irregular boundary, into a numerical domain with a flat bottom surface. Such a

https://doi.org/10.1121/10.0001766

procedure has already been used with the 2D PE, first by Beilis and Tappert (1979). The 3D Beilis-Tappert mapping can be defined as

$$\begin{aligned}\xi &= x,\\ \nu &= y,\\ \eta &= z - h(x,y),\end{aligned} \tag{5}$$

where $\boldsymbol{\xi} = (\xi, \nu, \eta)$ are the coordinates of the transformed domain and h is the boundary profile. It is worth noting that the terrain profile h can be expressed in either coordinate system. To proceed, the spatial derivatives in the physical coordinate system $\mathbf{x} = (x_i) = (x, y, z)$ are replaced using the chain rule, as

$$\frac{\partial}{\partial x_i} = \sum_{k=1}^{3} \frac{\partial \xi_k}{\partial x_i}\frac{\partial}{\partial \xi_k}, \tag{6a}$$

$$\frac{\partial^2}{\partial x_i \partial x_j} = \sum_{k=1}^{3} \frac{\partial^2 \xi_k}{\partial x_i \partial x_j}\frac{\partial}{\partial \xi_k} + \sum_{k=1}^{3}\sum_{n=1}^{3} \frac{\partial \xi_k}{\partial x_i}\frac{\partial \xi_n}{\partial x_j}\frac{\partial^2}{\partial \xi_k \partial \xi_n}, \tag{6b}$$

where $\xi_1 = \xi$, $\xi_2 = \nu$, and $\xi_3 = \eta$. The chain rules given by Eqs. (6a) and (6b) are then used to express the spatial derivatives in Eq. (3) and obtain an equation for the complex pressure envelope ψ in the new coordinate system. Thus, Eq. (3) becomes

$$\begin{aligned}&2ik_0\left(\frac{\partial \psi}{\partial \xi} - \left(\frac{\partial h}{\partial \xi} + M_y\frac{\partial h}{\partial \nu} - M_z\right)\frac{\partial \psi}{\partial \eta} + M_y\frac{\partial \psi}{\partial \nu}\right)\\ &\quad + \Delta_\perp^* \psi + \delta k_{\text{eff}}^2 \psi = 0,\end{aligned} \tag{7}$$

where $M_z = v_z/c_0$, $M_y = v_y/c_0$, and $\Delta_\perp^*$ is the transversal Laplacian operator, expressed in the transformed coordinate system (ξ, ν, η), given by

$$\Delta_\perp^* = \frac{\partial^2}{\partial \eta^2} + \left(\frac{\partial h}{\partial \nu}\right)^2\frac{\partial^2}{\partial \eta^2} + \frac{\partial^2}{\partial \nu^2} - \frac{\partial^2 h}{\partial \nu^2}\frac{\partial}{\partial \eta} - 2\frac{\partial h}{\partial \nu}\frac{\partial^2 \psi}{\partial \eta \partial \nu}. \tag{8}$$

After inspecting Eq. (7), it appears that the coordinate transformation in Eq. (5) has introduced a number of additional terms. Equation (7) can be further simplified by assuming all terms in the Laplacian containing derivatives of h to be negligible, which holds if the terrain varies slowly in the transversal direction. This assumption is consistent with the narrow-angle approximation, which limits the accuracy of the Beilis-Tappert mapping to sloping angles of 20° (Parakkal *et al.*, 2012). Therefore,

$$\Delta_\perp^* \approx \frac{\partial^2}{\partial \eta^2} + \frac{\partial^2}{\partial \nu^2}. \tag{9}$$

Grouping derivatives direction-wise, the narrow-angle 3D PE given by Eq. (7) becomes

$$\frac{\partial \psi}{\partial \xi} = \frac{ik_0}{2}(\mathcal{Z}^* + \mathcal{Y}^*)\psi \tag{10}$$

in the new coordinate system (ξ, ν, η), where the transformed differential operators $\mathcal{Z}^*$, $\mathcal{Y}^*$ are given by

$$\mathcal{Z}^* = \frac{1}{k_0^2}\frac{\partial^2}{\partial \eta^2} + \frac{\delta k_{\text{eff}}^2}{k_0^2} - \frac{2i}{k_0}\left(\frac{\partial h}{\partial \xi} + M_y\frac{\partial h}{\partial \nu} - M_z\right)\frac{\partial}{\partial \eta}, \tag{11a}$$

$$\mathcal{Y}^* = \frac{1}{k_0^2}\frac{\partial^2}{\partial \nu^2} + \frac{2iM_y}{k_0}\frac{\partial}{\partial \nu}. \tag{11b}$$

The operators in Eqs. (11a) and (11b) include atmospheric refraction in three geometrical directions. However, wind is usually assumed to be horizontal in a realistic atmosphere, so the z-component of the wind velocity can be neglected and $M_z = 0$. For a homogeneous atmosphere, the propagation medium is motionless and $M_z = M_y = 0$. The PE derived in Eq. (10) is a 3D counterpart of the 2D Beilis-Tappert PE derived by Parakkal *et al.* (2012),

$$\frac{\partial \phi}{\partial \xi} = \frac{i}{2k_0}\left(\frac{\partial^2 \phi}{\partial \eta^2} + \delta k_{\text{eff}}^2 \phi\right) - ik_0 \eta \frac{dh}{d\xi}\phi, \tag{12}$$

where ϕ is a modulated complex pressure given by $\phi = \psi e^{-i\theta}$ and θ is a phase shift defined as

$$\theta(\xi, \eta) = k_0\eta + \frac{k_0}{2}\int_0^\xi \left(\frac{dh}{d\xi}\right)^2 d\xi. \tag{13}$$

The 2D BTPE in Eq. (12) can be obtained from Eq. (10) by assuming a motionless medium ($\mathbf{v} = \mathbf{0}$) and an invariant complex pressure along ν. Therefore, the formulation in Eq. (10) is expected to correctly account for out-of-plane scattering from irregular boundaries (obstacles, terrain, etc.) and horizontal refraction from crosswinds.

The narrow-angle BTPE in Eq. (12) is also related to the GTPE) derived by Sack and West (1995). The main advantage of the Beilis-Tappert coordinate transform, given by Eq. (5), is the considerable simplification of the impedance boundary condition at the ground surface. Other formulations of the 3D PE, especially in the context of underwater acoustics, rely on an extended reacting model, where the ground material is characterized by a density ρ_g and sound speed c_g (Zhu and Bjørnø, 2000).

C. Approximate impedance boundary condition

The ground surface (i.e., the interface between the ground material and the atmosphere) is governed by a 3D IBC of the form

$$(\mathbf{n} \cdot \nabla)p = \frac{ik_0}{Z_g}p, \tag{14}$$

where Z_g is the ground surface impedance and $\mathbf{n} \cdot \nabla$ is the directional derivative taken along the normal vector $\mathbf{n}$. At

the ground boundary, defined by the 2D surface $\partial\mathcal{P}: \{\mathcal{S}(x,y,z) = h(x,y) - z = 0\}$, the unit normal vector is given by

$$\mathbf{n} = \frac{\nabla\mathcal{S}}{|\nabla\mathcal{S}|} = \frac{(\tan\theta_x, \tan\theta_y, -1)^T}{|\nabla\mathcal{S}|}, \tag{15}$$

where $\mathcal{S}$ is the equation of the ground surface, θ_x is the terrain slope along x, and θ_y is the transversal terrain slope along y (i.e., $\tan\theta_x = \partial h/\partial x$ and $\tan\theta_y = \partial h/\partial y$). So, inserting Eq. (15) into Eq. (14) leads to

$$\tan\theta_x\left(\frac{\partial p}{\partial x}\right) + \tan\theta_y\left(\frac{\partial p}{\partial y}\right) - \left(\frac{\partial p}{\partial z}\right) = ik_0 Y_g |\nabla\mathcal{S}| p, \tag{16}$$

where $Y_g = 1/Z_g$ is the ground admittance. Using the relation $p = e^{ik_0 x}\psi$ results in the following 3D IBC for the complex pressure envelope ψ,

$$\tan\theta_x\left(\frac{\partial \psi}{\partial x}\right) + \tan\theta_y\left(\frac{\partial \psi}{\partial y}\right) - \left(\frac{\partial \psi}{\partial z}\right) = ik_0 Y'_g \psi, \tag{17}$$

where $Y'_g = |\nabla\mathcal{S}|/Z_g - \tan\theta_x$. To use the above IBC in the 3D PE, one first needs to express the equation in the shifted coordinate system. At the ground level (i.e., at $\eta = 0$) we have $k = k_0$ and the density is $\rho(0) = \rho_0$ so the impedance boundary condition in the shifted coordinate system (ξ, ν, η) is

$$\begin{aligned}&\tan\theta_x\left(\frac{\partial \psi}{\partial \xi}\right) + \tan\theta_y\left(\frac{\partial \psi}{\partial \nu}\right)\\ &\quad -(\tan^2\theta_x + \tan^2\theta_y - 1)\left(\frac{\partial \psi}{\partial \eta}\right) = ik_0 Y'_g \psi,\end{aligned} \tag{18}$$

which is valid at the interface $\eta = 0$. Equation (18) includes derivatives with respect to ξ and ν that were not present in the case of a flat boundary, which makes the boundary condition more difficult to implement in the numerical scheme. This is due to the non-orthogonality of the coordinate transform since the grid is not normal to the bottom boundary. In Parakkal *et al.* (2010), the use of a polar conformal mapping allowed for an equivalent IBC that has a form $\partial\psi/\partial\eta = ik_0 Y_g + \chi/2$, where χ is the local curvature of the ground surface. In the present method, the staircase approximation is used, and the ground is assumed to be locally flat, which leads to $\theta_x = \theta_y \approx 0$ in Eq. (18). Furthermore, $Y'_g = Y_g = 1/Z_g$ and the impedance boundary condition becomes

$$\left(\frac{\partial \psi}{\partial \eta}\right)_{\eta=0} = ik_0 Y_g (\psi)_{\eta=0}. \tag{19}$$

The boundary condition given by Eq. (19) will be used to evaluate the pressure field ψ at $\eta = 0$ in the new coordinate system. The ground impedance Z_g contains information about the surface micro-structure and response to a traveling sound wave. Many theoretical and experimental models for porous grounds are given by Attenborough *et al.* (2011), usually involving several physical parameters, such as density, porosity, and flow resistivity.

D. Starting field

To solve the problem numerically, an initial condition on the complex pressure ψ at $\xi = 0$ is required. In many problems in atmospheric acoustics and infrasound, acoustic sources are modeled by monopole sources. In the context of the PE, the usual approach consists in choosing $\psi = \psi_0$, at $\xi = 0$, in such a way that the resulting solution exhibits spherical spreading and directivity in the far-field. Salomons (2001) gives the following Gaussian starter for the 2D PE,

$$\psi_0(z) = \sqrt{k_0}\exp\left(-\frac{(z - z_s)^2}{2k_0^2}\right). \tag{20}$$

A similar initial condition can be obtained for the 3D PE by extending the derivation given in Jensen *et al.* (2011), leading to

$$\psi_0(y,z) = k_0\exp\left(-\frac{(z - z_s)^2}{2k_0^2}\right) \times \exp\left(-\frac{(y - y_s)^2}{2k_0^2}\right). \tag{21}$$

The expression in Eq. (21) will be used in Sec. V to validate the 3D BTPE against BEM simulations.

III. NUMERICAL SCHEME

Along the propagation direction ξ, the field is discretized into N_ξ points $\xi_1, \ldots, \xi_{N_\xi}$, so the waveguide consists of a succession of N_ξ transversal planes, as shown in Fig. 1. In altitude, the domain is discretized into N_η points $\eta_1, \ldots, \eta_{N_\eta}$ and, transversally, into N_ν points $\nu_1, \ldots, \nu_{N_\nu}$. The value of ψ at the grid point (ξ_m, ν_j, η_n) is $\psi^m_{n,j}$ and $\Psi^m = (\psi^m_{n,j})_{n,j}$ is the matrix of the values of ψ in the plane $\xi = \xi_m$,

$$\Psi^m = \begin{pmatrix} \psi^m_{1,1} & \psi^m_{1,2} & \cdots & \psi^m_{1,N_\nu} \\ \psi^m_{2,1} & \psi^m_{2,2} & \cdots & \psi^m_{2,N_\nu} \\ \vdots & \vdots & \ddots & \vdots \\ \psi^m_{N_\eta,1} & \psi^m_{N_\eta,2} & \cdots & \psi^m_{N_\eta,N_\nu} \end{pmatrix}. \tag{22}$$

For the 3D PE, a marching scheme can be derived for $\mathbf{V}^m = \mathrm{vec}(\Psi^m)$, which is a vector of size $(N_\nu \times N_\eta)$ obtained by stacking the columns of Ψ^m (Sturm and Kampanis, 2007), i.e.,

$$\mathbf{V}^m = (\psi^m_{1,1}, \ldots, \psi^m_{N_\eta,1}, \ldots, \psi^m_{n,j}, \ldots \psi^m_{N_\eta,N_\nu})^T.$$

A direct finite-difference solution requires the inversion of a sparse system of a size $N_{3D} = N_\eta \times N_\nu$, leading to prohibitive scales for larger domains. To avoid such difficulty, the

https://doi.org/10.1121/10.0001766

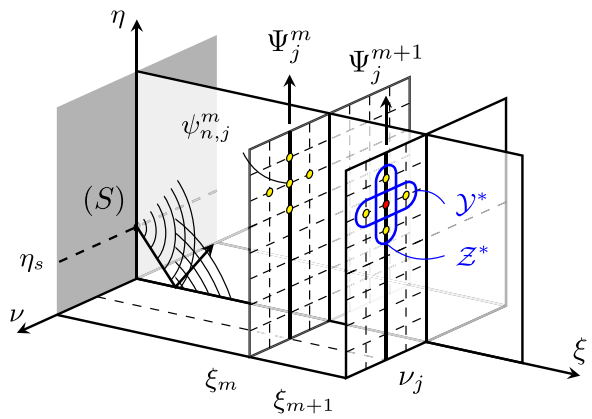

FIG. 1. (Color online) Discretization of the numerical domain $\mathcal{D}^*$ into a Cartesian grid of size $N_\xi \times N_\nu \times N_\eta$, where $\psi_{n,j}^m$ is the value of the complex envelope ψ at the grid point (ξ_m, ν_j, η_n).

3D PE is usually solved using tailored iterative solutions that take advantage of the matrix structure and reduce the amount of memory required. In this section, the narrow-angle 3D BTPE derived in Eq. (10) is solved using an iterative fixed-point method (Zelley and Constantinou, 1999), which seeks the solution at ξ_{m+1} by a recursive refinement of the solution at ξ_m. The advantage of this method is that it can generate an arbitrarily accurate solution, as long as a stability condition is met.

The remainder of this section is structured as follows: in Sec. III A, the numerical solution is obtained by discretizing the governing equation using finite-differences. In Sec. III B, the boundary conditions are discretized at the boundary points. In Sec. III C, an absorbing layer is defined for the damping of reflections from the domain boundaries. In Sec. III D, the marching scheme is written in matrix form, leading to a linear system. In Sec. III E, the iterative fixed-point algorithm is outlined and the stability condition discussed.

A. Finite-difference discretization

The 3D BTPE, given in Eq. (10), is solved by marching the solution in the direction ξ, starting from an initial value in the source plane $\xi = 0$. Assuming that ψ is known at a given range ξ, the field can be determined at $\xi + \Delta\xi$, and so on, until the wave has propagated through the whole domain. Between ξ_m and $\xi_{m+1} = \xi_m + \Delta\xi$, the marching scheme takes the incremental form (Lee and McDaniel, 1988),

$$\psi^{m+1} = \exp\left\{\Delta\xi \frac{\partial}{\partial\xi}\right\}\psi^m, \tag{23}$$

where $\psi^m = \psi(\xi_m)$ is a known field and $\psi^{m+1} = \psi(\xi_{m+1})$ is to be computed. After inserting Eq. (10) into Eq. (23), the range derivative is replaced and the following equation is obtained

$$\psi^{m+1} = \exp\left\{\frac{ik_0\Delta\xi}{2}(\mathcal{Z}^* + \mathcal{Y}^*)\right\}\psi^m. \tag{24}$$

The Crank-Nicholson method is applied to Eq. (24), which leads to

$$\exp\left\{-\frac{ik_0\Delta\xi}{4}(\mathcal{Z}^* + \mathcal{Y}^*)\right\}\psi^{m+1} = \exp\left\{\frac{ik_0\Delta\xi}{4}(\mathcal{Z}^* + \mathcal{Y}^*)\right\}\psi^m. \tag{25}$$

The exponential operators in Eq. (25) are then approximated using a first-order Taylor approximation, which yields the following marching scheme:

$$\{1 + \mu_0^-(\mathcal{Z}^* + \mathcal{Y}^*)\}\psi^{m+1} = \{1 + \mu_0^+(\mathcal{Z}^* + \mathcal{Y}^*)\}\psi^m, \tag{26}$$

where $\mu_0^\pm = \pm ik_0\Delta\xi/4$. Evaluating the semi-discretized marching scheme, defined in Eq. (26), at a transversal grid point $\boldsymbol{\xi}_\perp = (\nu_j, \eta_n)$ leads to the following system:

$$\begin{aligned} &B_{2,j,n}^-\left(\frac{\partial^2\psi}{\partial\nu^2}\right)_{n,j}^{m+1} + A_{2,j,n}^-\left(\frac{\partial^2\psi}{\partial\eta^2}\right)_{n,j}^{m+1} \\ &\quad + B_{1,j,n}^-\left(\frac{\partial\psi}{\partial\nu}\right)_{n,j}^{m+1} + A_{1,j,n}^-\left(\frac{\partial\psi}{\partial\eta}\right)_{n,j}^{m+1} + A_{0,j,n}^-\psi_{n,j}^{m+1} \\ &= B_{2,j,n}^+\left(\frac{\partial^2\psi}{\partial\nu^2}\right)_{n,j}^{m} + A_{2,j,n}^+\left(\frac{\partial^2\psi}{\partial\eta^2}\right)_{n,j}^{m} \\ &\quad + B_{1,j,n}^+\left(\frac{\partial\psi}{\partial\nu}\right)_{n,j}^{m} + A_{1,j,n}^+\left(\frac{\partial\psi}{\partial\eta}\right)_{n,j}^{m} + A_{0,j,n}^+\psi_{n,j}^m, \end{aligned} \tag{27}$$

where the spatially varying coefficients $A_2^\pm$, $A_1^\pm$, $A_0^\pm$ and $B_2^\pm$ in Eq. (27) are defined as

$$A_{0,j,n}^\pm = 1 + \frac{\mu_0^\pm}{k_0^2}(k_n^2 - k_0^2), \tag{28a}$$

$$A_{1,j,n}^\pm = -\frac{2i\mu_0^\pm}{k_0}\left(\frac{\partial h}{\partial\xi}\right)_{m,j} - \frac{2i\mu_0^\pm}{k_0}\left(M_{y,n}\left(\frac{\partial h}{\partial\nu}\right)_{m,j} - M_{z,n}\right), \tag{28b}$$

$$A_{2,j,n}^\pm = \frac{\mu_0^\pm}{k_0^2}, \tag{28c}$$

$$B_{1,j,n}^\pm = \frac{2i\mu_0^\pm}{k_0}M_{y,n}, \tag{28d}$$

$$B_{2,j,n}^\pm = \frac{\mu_0^\pm}{k_0^2}, \tag{28e}$$

where $k_n = k_{\text{eff}}(\eta_n)$. The first-order and second-order spatial derivatives of the wave field ψ in Eq. (27) are discretized using finite-differences. At a given grid point (ξ_m, ν_j, η_n), where $m = 1, \ldots, N_\xi$, $j = 1, \ldots, N_\nu$, and $n = 1, \ldots, N_\eta$, the

first- and second-order spatial derivatives with respect to the altitude η are given by Fornberg (1988):

$$\left(\frac{\partial^2\psi}{\partial\eta^2}\right)^m_{n,j} = \frac{\psi^m_{n+1,j} - 2\psi^m_{n,j} + \psi^m_{n-1,j}}{\Delta\eta^2}, \tag{29a}$$

$$\left(\frac{\partial\psi}{\partial\eta}\right)^m_{n,j} = \frac{\psi^m_{n+1,j} - \psi^m_{n-1,j}}{2\Delta\eta}, \tag{29b}$$

where $\Delta\eta = \eta_{n+1} - \eta_n$ is the uniform grid spacing. Similarly, the first-order and second-order derivatives in the transversal direction ν are defined as

$$\left(\frac{\partial^2\psi}{\partial\nu^2}\right)^m_{n,j} = \frac{\psi^m_{n,j+1} - 2\psi^m_{n,j} + \psi^m_{n,j-1}}{\Delta\nu^2}, \tag{30a}$$

$$\left(\frac{\partial\psi}{\partial\nu}\right)^m_{n,j} = \frac{\psi^m_{n,j+1} - \psi^m_{n,j-1}}{2\Delta\nu}. \tag{30b}$$

Inserting the finite-difference formulas, given in Eqs. (29a) to (30b), into Eq. (27) gives rise to a 10-point discrete system, containing $\psi^m_{n,j}$, $\psi^{m+1}_{n,j}$, and their four neighboring points,

$$\sum_{d=-1}^{1} M^-_{d,n,j}\psi^{m+1}_{n+d,j} + \sum_{d=-1}^{1} P^-_{d,n,j}\psi^{m+1}_{n,j+d} = \sum_{d=-1}^{1} M^+_{d,n,j}\psi^m_{n+d,j} + \sum_{d=-1}^{1} P^+_{d,n,j}\psi^m_{n,j+d}, \tag{31}$$

for $j = 1,\ldots,N_\nu$ and $n = 1,\ldots,N_\eta$. The finite-difference weights $M^\pm_{d,n,j}$ and $P^\pm_{d,n,j}$ in Eq. (31) are given by

$$M^\pm_{-1,n,j} = \frac{A^\pm_{2,j,n}}{\Delta\eta^2} - \frac{A^\pm_{1,j,n}}{2\Delta\eta}, \tag{32a}$$

$$M^\pm_{0,n,j} = \frac{-2A^\pm_{2,j,n}}{\Delta\eta^2} + A^\pm_{0,j,n}, \tag{32b}$$

$$M^\pm_{1,n,j} = \frac{A^\pm_{2,j,n}}{\Delta\eta^2} + \frac{A^\pm_{1,j,n}}{2\Delta\eta}, \tag{32c}$$

and

$$P^\pm_{-1,n,j} = \frac{B^\pm_{2,j,n}}{\Delta\nu^2} - \frac{B^\pm_{1,j,n}}{2\Delta\nu}, \tag{33a}$$

$$P^\pm_{0,n,j} = \frac{-2B^\pm_{2,j,n}}{\Delta\nu^2}, \tag{33b}$$

$$P^\pm_{1,n,j} = \frac{B^\pm_{2,j,n}}{\Delta\nu^2} + \frac{B^\pm_{1,j,n}}{2\Delta\nu}. \tag{33c}$$

B. Boundary conditions

Next, the boundary conditions at the edges of the numerical domain are discretized. At the domain limit points $n = 1$ (bottom boundary), $n = N_\eta$ (top boundary), $j = 1$ (left boundary), and $j = N_\nu$ (right boundary), the finite-difference formulas in Eqs. (29a) to (30b) will contain discrete values of ψ that are outside the numerical domain, as shown in Fig. 2. There is, therefore, a need for defining virtual points to enable the numerical scheme. The virtual points associated with each boundary are

$$\begin{aligned}
&\text{Bottom,} \quad \mathcal{D}_g: \quad \psi^m_{0,j}, \quad j = 1\cdots N_\nu\\
&\text{Top,} \quad \mathcal{D}_t: \quad \psi^m_{N_\eta+1,j}, \quad j = 1\cdots N_\nu\\
&\text{Left,} \quad \mathcal{D}_1: \quad \psi^m_{n,0}, \quad n = 1\cdots N_\eta\\
&\text{Right,} \quad \mathcal{D}_2: \quad \psi^m_{n,N_\nu+1}, \quad n = 1\cdots N_\eta
\end{aligned}$$

This leads to a total number of $N_{\text{bnd}} = 2(N_\eta + N_\nu)$ unknown virtual points, which must be expressed using the boundary conditions. At the bottom of the domain (i.e., at $\eta = 0$), the boundary condition is given by Eq. (19) for a ground of impedance Z_g. The top and side boundaries ($\eta = \eta_{\max}$ and $\nu = \nu_{\min}, \nu_{\max}$) are truncations of the propagation domain and are governed by an impedance $Z_0 = 1$, since the interface is made of air. We begin by dealing with the bottom boundary condition at $\eta = 0$ by inserting Eq. (29b) into the discretized flat IBC defined in Eq. (19), leading to

$$\frac{-\psi^m_{2,j} + 4\psi^m_{1,j} - 3\psi^m_{0,j}}{2\Delta\eta} = \frac{ik_0}{Z_g}\psi^m_{0,j}. \tag{34}$$

The top boundary condition at $\eta = \eta_{\max}$ is similarly defined by

$$\frac{-\psi^m_{N_\eta-1,j} + 4\psi^m_{N_\eta,j} - 3\psi^m_{N_\eta+1,j}}{2\Delta\eta} = \frac{ik_0}{Z_0}\psi^m_{N_\eta,j}. \tag{35}$$

The side boundary conditions will contain the same coefficients as Eq. (35). A schematic of the numerical domain and

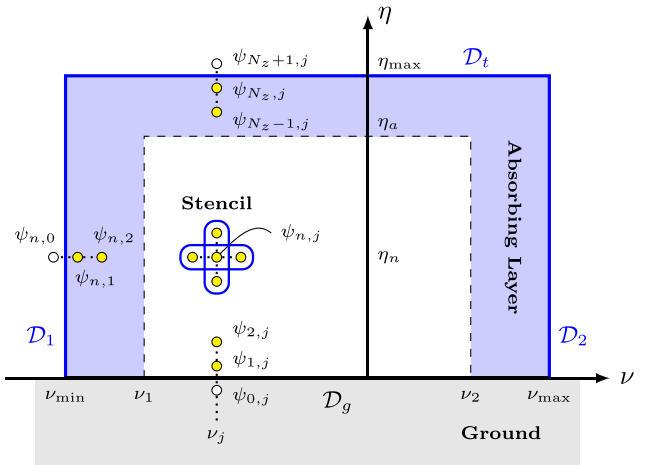

FIG. 2. (Color online) Transversal slice of the numerical grid, delimited by the edges $\mathcal{D}_t$ at the top, $\mathcal{D}_g$ at the bottom, $\mathcal{D}_1$ on the left (minimum cross-range), and $\mathcal{D}_2$ on the right (maximum cross-range). The finite-difference stencil at the point $\psi_{n,j}$ includes four neighboring points $\psi_{n+1,j}$, $\psi_{n-1,j}$, $\psi_{n,j-1}$, and $\psi_{n,j+1}$. The filled dots are solution points, and the empty dots are virtual points, at which boundary conditions are evaluated.

https://doi.org/10.1121/10.0001766

finite-difference stencils at the domain boundaries are presented in Fig. 2. Rearranging the coefficients of Eqs. (34) and (35) allows us to obtain a value for the virtual points, which will then be inserted into the finite-difference matrices. Thus, the virtual points $\psi^m_{0,j}$, $\psi^m_{N_\eta+1,j}$, $\psi^m_{n,0}$, and $\psi^m_{n,N_\nu+1}$ are given by

$$\psi^m_{0,j} = \alpha^g_1\psi^m_{1,j} + \alpha^g_2\psi^m_{2,j}, \tag{36a}$$

$$\psi^m_{N_\eta+1,j} = \alpha^t_1\psi^m_{N_\eta j} + \alpha^t_2\psi^m_{N_\eta-1,j}, \tag{36b}$$

$$\psi^m_{n,0} = \beta_1\psi^m_{n,1} + \beta_2\psi^m_{n,2}, \tag{36c}$$

$$\psi^m_{n,N_\nu+1} = \beta_1\psi^m_{n,N_\nu} + \beta_2\psi^m_{n,N_\nu-1}, \tag{36d}$$

where the constant coefficients α^t_1, α^t_2, α^g_1, and α^g_2 are given by

$$\alpha^t_1 = 4/(3 + 2ik_0\Delta\eta), \tag{37a}$$

$$\alpha^t_2 = -1/(3 + 2ik_0\Delta\eta), \tag{37b}$$

$$\alpha^g_1 = 4Z_g/(3Z_g - 2ik_0\Delta\eta), \tag{37c}$$

$$\alpha^g_2 = -Z_g/(3Z_g - 2ik_0\Delta\eta), \tag{37d}$$

and β_1, β_2 are given by

$$\beta_1 = 4/(3 + 2ik_0\Delta\nu), \tag{38a}$$

$$\beta_2 = -1/(3 + 2ik_0\Delta\nu). \tag{38b}$$

For a rigid surface, the surface impedance is $Z_g = \infty$, leading to $\alpha^g_1 = 4/3$ and $\alpha^g_2 = -1/3$.

C. Domain truncation and absorbing layer

The numerical domain $\mathcal{D}$, shown in Fig. 2, is truncated in order to limit reflections from the boundary limits. Following Salomons (2001), waves can be artificially damped by introducing an artificial absorbing layer. This is achieved by making use of a complex wavenumber, $\tilde{k} = k_{\text{eff}} + i\kappa$, in an absorbing layer that is placed far from the receiver location. The absorbing layer is placed inside the numerical domain $\mathcal{D}$ just before the outer boundaries, above the altitude η_a and transversally beyond ν_1 and ν_2, as shown in Fig. 2. The general expression of the wavenumber k in the 3D BTPE, given in Eq. (10), can be synthesized as $\tilde{k}(\eta,\nu) = k_{\text{eff}}(\eta) + i\kappa_{\text{side}}(\nu) + i\kappa_{\text{top}}(\eta)$, where the function κ_{side} and κ_{top} are the side and top absorbing functions. Here, the following profiles are used:

$$\kappa_{\text{side}}(\nu) = \kappa_0 \times \begin{cases} \left(\dfrac{\nu-\nu_2}{\nu_{\max}-\nu_2}\right)^2, & \nu \geq \nu_2, \\ \left(\dfrac{\nu-\nu_1}{\nu_1-\nu_{\min}}\right)^2, & \nu \leq \nu_1, \\ 0, & \nu_1 \leq \nu \leq \nu_2, \end{cases} \tag{39}$$

for the side absorbing layer, where ν_1, ν_2, $\nu_{\min}$, and $\nu_{\max}$ are the side absorbing layer limits, as shown in Fig. 2, and

$$\kappa_{\text{top}}(\eta) = \kappa_0 \times \begin{cases} \left(\dfrac{\eta-\eta_a}{\eta_{\max}-\eta_a}\right)^2, & \eta \geq \eta_a, \\ 0, & \eta \leq \eta_a, \end{cases} \tag{40}$$

for the top absorbing layer, where η_a and $\eta_{\max}$ are the top absorbing layer limits, as shown in Fig. 2. In Eqs. (39) and (40), κ_0 is an absorbing coefficient. For a large enough value of the layer thickness, spurious reflections can be made negligible. Inserting Eqs. (39) and (40) into the imaginary part of k_{eff} in the operator $\mathcal{Z}^*$, given by Eq. (11a), changes the value of the coefficient A_0 in Eq. (28a) to

$$A^{\pm}_{0,n,j} = 1 + \frac{\mu^{\pm}_0}{k_0^2}\left(\tilde{k}^2_{n,j} - k_0^2\right), \tag{41}$$

where $\tilde{k}$ is the complex wavenumber in the absorbing region, defined by $\tilde{k}_{n,j} = \tilde{k}(\eta_n,\nu_j)$. The coefficients $A^{\pm}_0$ now include transversal dependency in the side absorbing regions and must be updated for every column computation. The value of the artificial absorbing coefficient κ_0 is frequency-dependent and must be kept as small as possible so as to limit reflection from the absorbing layer interfaces. It is, therefore, preferable to increase the size of the absorbing layer in both η and ν directions rather than increase the artificial absorbing coefficient κ_0.

D. Matrix equation

The discretized marching scheme, derived in Eq. (27), is then written in matrix form by assembling all the discretized values $\psi^m_{n,j}$, in the propagation plane ξ_m, into a matrix Ψ^m as in Eq. (22). In matrix form, the numerical scheme derived in Eq. (27) reduces to a matrix equation relating the unknown field $\Psi^{m+1} = (\psi^{m+1}_{n,j})_{n,j}$ at step $m+1$ to the solution Ψ^m computed at the previous step. The numerical scheme can be written in a more convenient form by considering each column of the propagation field Ψ^m separately. Consequently, Eq. (27) is equivalent to N_ν linear systems of the form

$$\mathbf{\Phi}^m = \{\boldsymbol{\psi}^m_n \mathbf{P}^+_n\}, \tag{42a}$$

$$\mathbf{\Phi}^{m+1} = \{\boldsymbol{\psi}^{m+1}_n \mathbf{P}^-_n\}, \tag{42b}$$

$$\mathbf{M}^-_j \Psi^{m+1}_j + \Phi^{m+1}_j = \mathbf{M}^+_j \Psi^m_j + \Phi^m_j, \tag{42c}$$

where Ψ^m_j is the j-th column of the field $\mathbf{\Psi}^m$ and $\boldsymbol{\psi}^m_n$ denotes the n-th row of Ψ^m. The bracket notation introduced in Eqs. (42a) and (42b) signifies that the dummy matrices $\mathbf{\Phi}^m$ and $\mathbf{\Phi}^{m+1}$ are computed row by row. The finite-difference matrices $\mathbf{M}^{\pm}_j$ in Eq. (42c) operate on the columns of the field matrices and depend on the transversal index j. $\mathbf{M}^{\pm}_j$ are tridiagonal, with a size N_η and given by

$$\mathbf{M}_j^{\pm} = \begin{pmatrix} E_{0,j}^{\pm} & E_{1,j}^{\pm} & & & & \\ M_{-1,2,j}^{\pm} & M_{0,2,j}^{\pm} & M_{1,2,j}^{\pm} & & & \\ & \ddots & \ddots & \ddots & & \\ & & \ddots & \ddots & M_{1,N_\eta-1,j}^{\pm} & \\ & & & F_{-1,j}^{\pm} & F_{0,j}^{\pm} & \end{pmatrix}. \tag{43}$$

At the interior grid points, which correspond to the row indexes $n = 2, \ldots, N_\eta - 1$, the coefficients $M_{d,n,j}^{\pm}$ are given in Eqs. (32a) to (32c). At the boundary points $n = 1$ and $n = N_\eta$, the coefficients $E^{\pm}$ and $F^{\pm}$ are defined by

$$E_{0,j}^{\pm} = M_{0,1,j}^{\pm} + \alpha_1^g M_{-1,1,j}^{\pm}, \tag{44a}$$

$$E_{1,1,j}^{\pm} = M_{1,1,j}^{\pm} + \alpha_2^g M_{-1,1,j}^{\pm}, \tag{44b}$$

$$F_{-1,j}^{\pm} = M_{-1,N_\eta,j}^{\pm} + \alpha_2^t M_{1,N_\eta,j}^{\pm}, \tag{44c}$$

$$F_{0,j}^{\pm} = M_{0,N_\eta,j}^{\pm} + \alpha_1^t M_{1,N_\eta,j}^{\pm}, \tag{44d}$$

where α_1^g, α_2^g, α_1^t, and α_2^t are defined in Eqs. (37a) to (37d). In Eqs. (42a) and (42b), the matrices $\mathbf{P}_n^{\pm}$ operate on the rows of the field matrices and depend on the altitude index n. These matrices are of size N_ν and are given by

$$\mathbf{P}_n^{\pm} = \begin{pmatrix} G_{0,n}^{\pm} & G_{1,n}^{\pm} & & & & \\ P_{-1,2,n}^{\pm} & P_{0,2,n}^{\pm} & P_{1,2,n}^{\pm} & & & \\ & \ddots & \ddots & \ddots & & \\ & & \ddots & \ddots & P_{1,N_\nu-1,n}^{\pm} & \\ & & & H_{-1,n}^{\pm} & H_{0,n}^{\pm} & \end{pmatrix}. \tag{45}$$

At the interior grid points, which correspond to the column indexes $j = 2, \ldots, N_\nu - 1$, the coefficients $P_{d,n,j}^{\pm}$ are defined in Eqs. (33a) to (33c). At the boundary points $n = 1$ and $n = N_\eta$, the coefficients $M_{d,n,j}^{\pm}$ are defined by

$$G_{0,n}^{\pm} = P_{0,1,n}^{\pm} + \beta_1 P_{-1,1,n}^{\pm}, \tag{46a}$$

$$G_{1,n}^{\pm} = P_{1,1,n}^{\pm} + \beta_2 P_{-1,1,n}^{\pm}, \tag{46b}$$

$$H_{-1,n}^{\pm} = P_{-1,N_\nu,n}^{\pm} + \beta_2 P_{1,N_\nu,n}^{\pm}, \tag{46c}$$

$$H_{0,n}^{\pm} = P_{0,N_\nu,n}^{\pm} + \beta_1 P_{1,N_\nu,n}^{\pm}, \tag{46d}$$

where β_1 and β_2 are defined in Eqs. (38a) and (38b).

E. Iterative fixed-point scheme

The linear system in Eq. (42c) is a generalized Sylvester equation, which is a class of matrix equations of the form

$$\sum_i \mathbf{A_i} \mathbf{X} \mathbf{B_i} = \mathbf{C}, \tag{47}$$

for an unknown matrix $\mathbf{X}$ and rectangular matrices $\mathbf{A_i}$, $\mathbf{B_i}$, and $\mathbf{C}$. An extensive review of numerical methods for solving Eq. (47) is provided by Simoncini (2016). A particular method known as the gradient-based iterative scheme has been previously used by Zelley and Constantinou (1999) to solve the 3D PE for electromagnetic propagation above irregular terrain. The objective is to compute the unknown field $\mathbf{\Psi}^{m+1}$ at the range step ξ_{m+1}, by successive refinements $\mathbf{\Psi}^{(i)}$, where $i = 1, 2, 3, \ldots$, of the field $\mathbf{\Psi}^m$ computed at the previous step. This method can be viewed as a matrix formulation of the Jacobi iterative scheme (Van Loan and Golub, 1983), which is a well-known class of numerical solvers for parabolic partial differential equations. The algorithm to solve Eq. (42c) can be divided into four successive steps:

Step 1: Starting from the solution $\mathbf{\Psi}_m$ at step m, the matrix $\mathbf{\Phi}^m = \{\boldsymbol{\psi}_n^m \mathbf{P}_n^+\}$ is computed row by row. Then, the right-hand-side of Eq. (42c) is computed for $j = 1, \ldots, N_\nu$ and stored in the vectors C_j^m,

$$C_j^m = \mathbf{M}_j^+ \mathbf{\Psi}_j^m + \mathbf{\Phi}_j^m. \tag{48}$$

Step 2: Beginning with the initial guess $\mathbf{\Psi}^{(0)} = \mathbf{\Psi}^m$, the solution is successively refined, and we name $\mathbf{\Psi}^{(i)}$ the intermediate solution after i iterations. The matrix $\mathbf{\Phi}^{(i-1)} = \{\boldsymbol{\psi}_n^{(i-1)} \mathbf{P}_n^-\}$ is computed row by row, where $\boldsymbol{\psi}_n^{(i-1)}$ is the n-th row of the previous intermediate solution. Thus, using Eq. (42c), the j-th column $\Psi_j^{(i)}$ is computed by passing the second term to the right-hand-side,

$$\mathbf{M}_j^- \Psi_j^{(i)} \approx C_j^m - \Phi_j^{(i-1)}. \tag{49}$$

Step 3: The system in Eq. (49) is solved using a LU decomposition on the tridiagonal matrix $\mathbf{M}_j$, for $j = 1, \ldots, N_\nu$, which gives a solution for the columns $\Psi_j^{(i)}$. The intermediate field $\mathbf{\Psi}^{(i)}$ is obtained by grouping all the columns $\Psi_j^{(i)}$,

$$\mathbf{\Psi}^{(i)} = (\Psi_1^{(i)}, \Psi_2^{(i)}, \ldots, \Psi_{N_\nu}^{(i)}).$$

Step 4: The intermediate solution $\mathbf{\Psi}^{(i)}$ is considered acceptable if the convergence condition,

$$||\mathbf{\Psi}^{(i)} - \mathbf{\Psi}^{(i-1)}|| < \epsilon, \tag{50}$$

is met, in which case $\mathbf{\Psi}^{m+1} = \mathbf{\Psi}^{(i)}$, and the algorithm returns to Step 1 with m incremented to $m + 1$. If Eq. (50) is not met, the algorithm returns to Step 2, and the solution $\mathbf{\Psi}^{(i)}$ is refined again until convergence is observed. A typical value for the convergence threshold is $\epsilon = 10^{-4}$.

The stability of the iterative scheme for Eq. (42c) can be ensured as long as the matrices $\mathbf{M}_j^-$ and $\mathbf{P}_n^-$ verify the condition

$$||\mathbf{M}_j^-||^2 < 2 - ||\mathbf{P}_n^-||^2, \tag{51}$$

https://doi.org/10.1121/10.0001766

according to Xie *et al.* (2009). Zelley and Constantinou (1999) pointed out that Eq. (51) can be enforced heuristically by making the norm of the matrices $\mathbf{P}_n^-$ small enough in comparison with $\mathbf{M}_j^-$, which was achieved by transferring the constant diagonal elements of $\mathbf{P}_n^-$ to $\mathbf{M}_j^-$. The main advantage of this method over the ADI scheme is a better numerical accuracy, at the expense of a slower convergence. As shown in Fig. 3, a smaller grid size $\Delta\xi = \Delta\nu = \Delta\eta$ leads to a higher number of iterations before convergence. In practice, a good choice for $\Delta\xi$ is between $\lambda/8$ and $\lambda/20$, where $\lambda = c_0/f$ is the wavelength, so as to ensure that the central processing unit (CPU) time is kept under control.

IV. NUMERICAL EXAMPLES

In this section, a simple numerical example of infrasonic propagation is considered. While the solver developed in Sec. III includes atmospheric refraction, numerical simulations will be carried out for a homogeneous atmosphere, with a constant sound speed of $c_0 = 343$ m/s. In order to validate the method developed above, a boundary element solution, implemented in COMSOL Multiphysics, is used as a benchmark. A 2D BTPE solution is also computed in the middle plane $y = 0$. The propagation domain is a rectangular waveguide of size $10 \times 2 \times 2$ km,[3] delimited by $0 < x < 10$ km, $-1 < y < 1$ km, and $0 < z < 2$ km. The bottom boundary is a Gaussian hill, centered at $x_0 = 5$ km and $y_0 = 0$ km. The profile function is given by

$$h(x,y) = h_0 \exp\left(-\frac{(x-x_0)^2}{2s_x^2}\right)\exp\left(-\frac{(y-y_0)^2}{2s_y^2}\right), \tag{52}$$

where $h_0 = 200$ m and $s_x = s_y = 500$ m. A schematic of the propagation domain is given in Fig. 4. The maximum sloping angle of the hill is 19.6°, which is close to the theoretical limit of the narrow-angle BTPE (Parakkal *et al.*, 2012). A better estimate than the pressure p for the amplitude variation and spreading of an acoustic wave is the sound pressure level (SPL), defined by

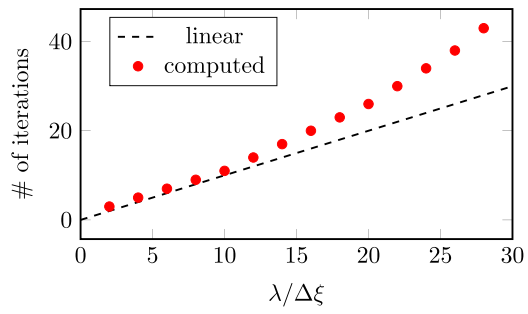

FIG. 3. (Color online) Variation of the average number of iterations N_{stp} as a function of the number of steps per wavelength $\lambda/\Delta\xi$, for a tolerance $\epsilon = 10^{-4}$. The computations are done in free-field with $f = 10$ Hz and $c_0 = 343$ m/s. The number of iterations vary quadratically with $\lambda/\Delta\xi$.

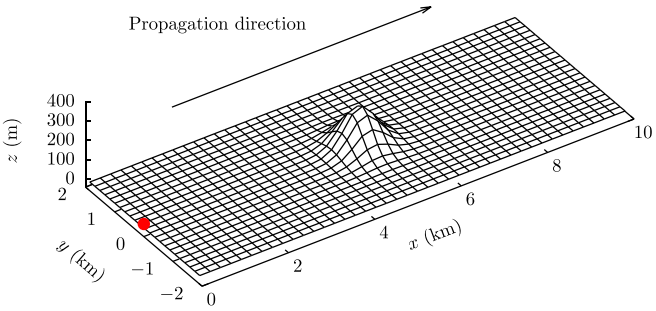

FIG. 4. (Color online) Schematic of the three-dimensional Gaussian hill. The red dot represents the location of the source (at altitude 25 m).

$$\hat{L}_p(\mathbf{x}) = 10\log_{10}\left(\frac{p_{\text{rms}}^2(\mathbf{x})}{p_{\text{ref}}^2}\right), \tag{53}$$

where p_{rms} is the root-mean-square pressure, defined as $p_{\text{rms}} = |p|/\sqrt{2}$ in the frequency-domain. The reference pressure p_{ref} is taken one numerical step away from the source in the x direction. The source is located at $\mathbf{x}_s = (0, 0, 25)$ m and has a strength $S_0 = 1$ Pa. Two frequencies are considered: $f = 1$ Hz and $f = 5$ Hz, with corresponding wavelengths $\lambda = c_0/f$ of 343 m and 68.6 m, respectively. At $f = 1$ Hz, the total domain range is 29λ, and the terrain height is equal to 0.58λ. At $f = 5$ Hz, the total range extends to 145λ, and the terrain height is 2.91λ. The artificial absorbing layer, defined in Sec. III C, is placed at the top of the domain, in the region $2 < z < 3$ km, and, on each side of the propagation domain, in the regions $-2 < y < -1$ km and $1 < y < 2$ km.

A. COMSOL model configuration

The COMSOL model is created with BEM physics interface in the Acoustics Module. Using the BEM interface presents a number of advantages over the traditional Finite Element Methods (FEM), as only the scattering objects (i.e., the Gaussian hill) need to be discretized with surface elements. The solution in the rest of the domain is calculated using the Kirchhoff-Helmholtz boundary integral:

$$\psi(\mathbf{x}) = \psi_i(\mathbf{x}) + \int\int_{\mathcal{S}} (\mathbf{n}\cdot\nabla)G(\mathbf{x},\mathbf{x}')\psi(\mathbf{x}')d\mathbf{x}', \tag{54}$$

where G is the 3D Green function, ψ_i is the incident field, and $\mathcal{S}$ is the scattering surface. The BEM typically reduces the size of the problem, since no volumetric mesh is needed. The mesh quality is controlled through the maximum element size, which is defined as $\lambda/8$, where λ is the wavelength. For $f = 1$ Hz, the number of degrees of freedom (DOFs) can be reduced to about 14×10^3 DOFs with the BEM and appropriate use of symmetry, instead of 4×10^6 DOFs with a standard FEM. In the simulations presented here, a GMRES iterative solver is used with a Sparse Approximate Inverse (SAI) preconditioning. The residual error for convergence is set to 10^{-3} and the rest of the parameters are left at their default values.

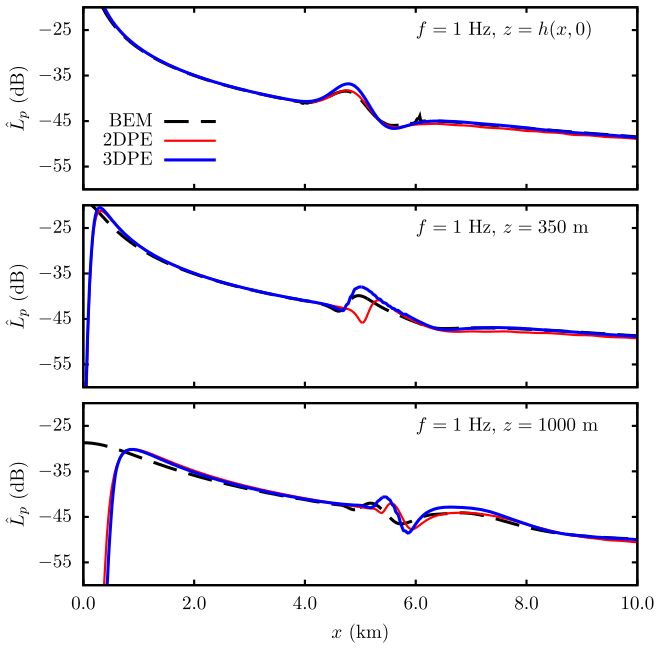

FIG. 5. (Color online) Variation of the SPL with range in the middle plane and for $f = 1$ Hz, taken along the ground surface (first row), the line $z = 350$ m (second row), and $z = 1$ km (third row).

B. Results and discussion

The results from the 3D BTPE for the Gaussian hill are compared against the BEM solution and the 2D BTPE. The SPL, defined in Eq. (53), is plotted in Figs. 5–7 for $f = 1$ Hz, and Figs. 8–10 for $f = 5$ Hz.

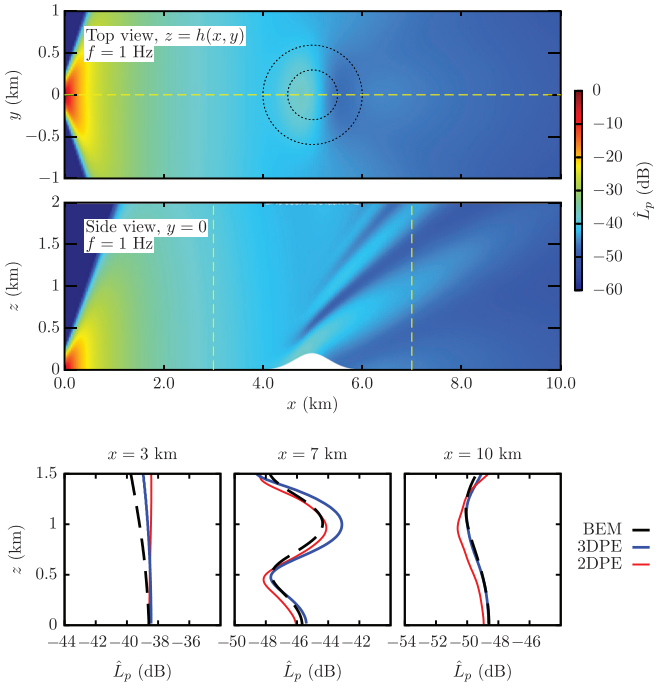

FIG. 6. (Color online) 3D BTPE solution of the propagation above the Gaussian hill at $f = 1$ Hz. The first row shows the SPL at the ground surface. The second row shows the SPL in the middle plane $y = 0$. The third row shows the SPL along the lines $x = 3$, 7, and 10 km in the middle plane.

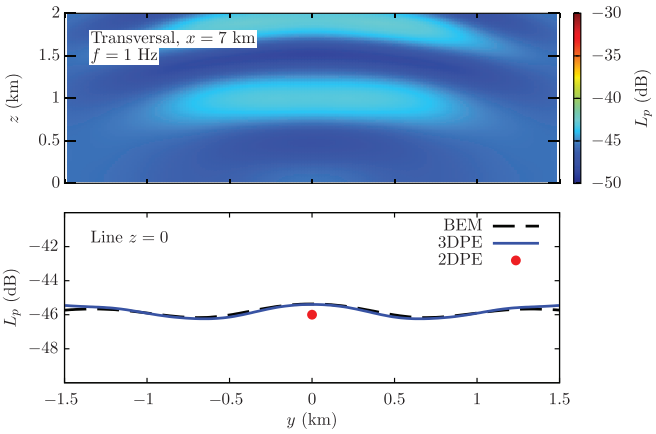

FIG. 7. (Color online) Transversal variation of the SPL at $x = 7$ km and $f = 1$ Hz. The first row shows the contour plot of the 3D BTPE solution in the plane $x = 7$ km. The second row shows the SPL along the transversal line $z = 0$ at $x = 7$ km.

Figure 5 shows the SPL variation, for $f = 1$ Hz, along x in the middle plane $y = 0$ and at several altitudes. The presence of the obstacle causes an increase in SPL upstream of the hill ($x < 5.0$ km) and a shadow zone downstream of the hill ($x > 5.0$ km). At $z = 350$ m (second panel of Fig. 5), the 2D solution shows an error of about 7 dB with BEM at 5.0 km, suggesting that 3D effects do not occur only in the shadow zone, but at the vicinity of the peak as well. Contour plots of the SPL at the ground surface and in the middle plane are given in Fig. 6, where it appears that the reflected wave leads to destructive interferences at higher altitudes. The last row of Fig. 6 shows the altitude variation of the SPL at different ranges and indicates that the 3D BTPE correctly estimates the intensity of the scattered field close to

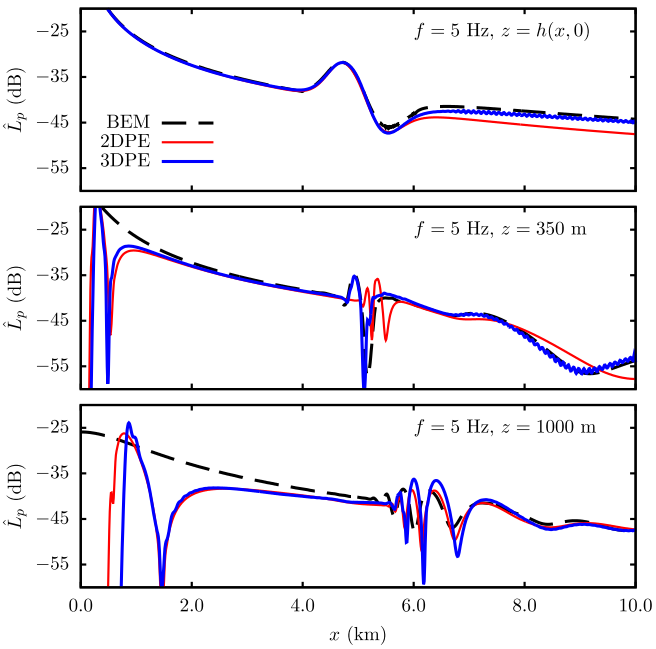

FIG. 8. (Color online) Variation of the SPL with range in the middle plane and for $f = 5$ Hz, taken along the ground surface (first row), the line $z = 350$ m (second row) and $z = 1$ km (third row).

https://doi.org/10.1121/10.0001766

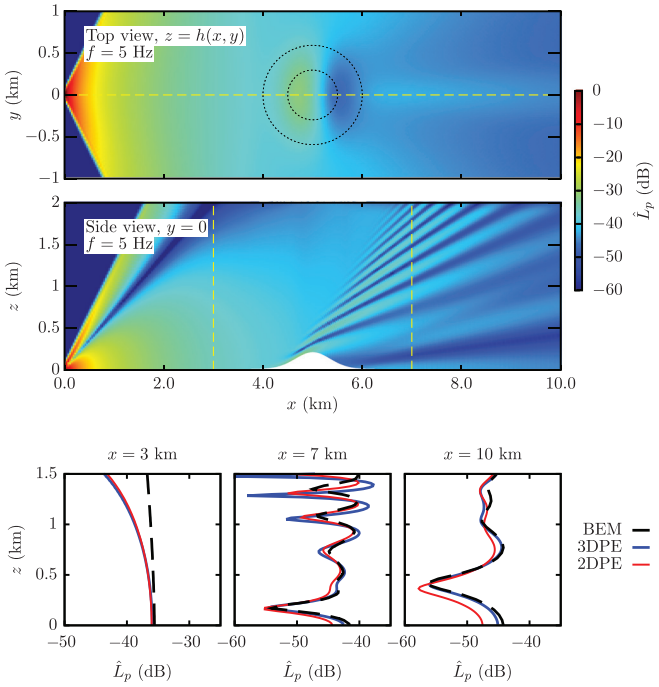

FIG. 9. (Color online) 3D BTPE solution of the propagation above the Gaussian hill at $f = 5$ Hz. The first row shows the SPL at the ground surface. The second row shows the SPL in the middle plane $y = 0$. The third row shows the comparison of the SPL along the lines $x = 3$, 7, and 10 km in the middle plane.

the ground. The transversal variation of the SPL at $x = 7.0$ km (i.e., just downstream of the hill) is shown in Fig. 7. Results show that the 3D BTPE matches the BEM closely. At this frequency, the effect of the hill on the acoustic wave amplitude is not significant, with both the 2D and 3D solutions very close to the BEM.

At $f = 5$ Hz, the ratio between the terrain height and the wavelength h_0/λ is larger than 1, which leads to a greater interaction between the obstacle and the incident wave. The SPL variation along x is shown in Fig. 8. The important discrepancy between the 3D BTPE and the BEM at short ranges is due to the paraxial approximation. In the far-field,

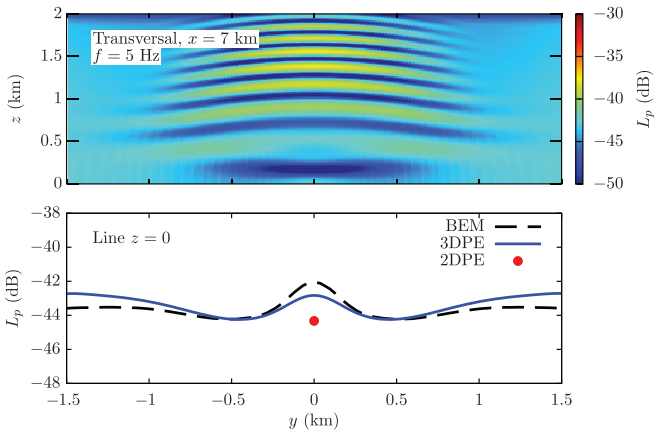

FIG. 10. (Color online) Transversal variation of the SPL at $x = 7$ km and $f = 5$ Hz. The first row shows the contour plot of the 3D BTPE solution in the plane $x = 7$ km. The second row shows the SPL along the transversal line $z = 0$ at $x = 7$ km.

the 3D BTPE agrees with the BEM very well, with a difference of ± 1 dB. Figure 9 shows the contour plot of the SPL at the ground surface and in the middle plane, as well as the variation of the SPL with altitude at different ranges. The contour plot in the middle plane shows a large number of interferences at higher altitude and a strong pressure decrease in the shadow zone. The 3D BTPE performs very well and captures 3D effects correctly. This is specifically visible in the last two plots of Fig. 9 (for $x = 7$ km and $x = 10$ km), where the 2D BTPE fails to properly account for the pressure increase in the shadow zone near the ground, by a margin of –4 dB. This pressure increase is explained by the presence of out-of-plane scattering due to the transversal variation of the hill. The transversal variation of the SPL at $x = 7.0$ km is shown in Fig. 10. Again, the 3D BTPE performs well and matches the BEM within a margin of 1 dB.

The presence of the pressure lobe in Fig. 9 is the result of destructive interference between the incident and reflected waves. This phenomenon is known as the Lloyd's mirror pattern and occurs when an acoustic source is placed close to, but not at, an impedance ground surface (Jensen *et al.*, 2011). The theory shows that the number of such interferences increases with frequency, which is why the pressure lobe is not observed at $f = 1$ Hz (cf. Figure 6).

Overall, results show a good agreement between the 3D PE and the BEM method, with a discrepancy that is smaller than 1 dB close to the ground, for both frequencies. The important discrepancies in the near-field and at higher altitudes are due to the paraxial approximation, constraining the validity of the PE solution to small propagation angles. In the far-field (at $x = 10$ km), the 3D BTPE matches the BEM almost exactly, and comparisons with the 2D solution highlight the presence of 3D effects at $f = 5$ Hz, which cause a difference of about 2 dB downstream of the obstacle, as shown in Fig. 10. The computational time of the 3D BTPE is approximately 50 times faster than the BEM simulations, with a total CPU time of around 5 min for $f = 5$ Hz against 4 h and 20 min for the COMSOL model. At $f = 5$Hz, the numerical domain has a cross-section $N_\eta \times N_\nu$ of 437×583 grid points and a total range of 1450 grid points. This results in a total of 369×10^6 DOFs on the whole numerical domain. The practical limit of the iterative fixed point scheme is, for N_η and N_ν, exceeding values of around 5000, above which the marching scheme becomes excessively slow (but still faster than BEM), with no impact on the convergence rate. For the Gaussian hill problem presented here, where the wave propagates over 10 km, computational times will start to exceed 24 h for $f \geq 50$ Hz.

V. CONCLUSIONS

In this paper, the Cartesian 3D PE has been extended to propagation above irregular boundaries. The method was derived by applying the Beilis-Tappert transform to the narrow-angle 3D PE in a layered moving atmosphere. The analysis carried out shows that the resulting equation, which is a 3D version of the Beilis-Tappert PE, can be efficiently solved

with an iterative fixed-point algorithm. As in 2D, the paraxial approximation inherent to the narrow-angle PE limits the model to irregular boundaries with slopes of about 20°. While this limitation still covers a large amount of practical cases, extending the method to wide-angle propagation with a non-flat impedance boundary condition is highly desirable.

Comparison against boundary elements shows a good agreement at low frequencies in homogeneous atmosphere. Furthermore, it has been shown that 3D effects occur in the shadow zone as a result of transversal scattering from the obstacle, resulting in an increase of nearly 2 dB compared to the 2D PE. This approach opens new possibilities for the modeling of long-range acoustic propagation in transversally varying waveguides, as the iterative fixed-point methods can be used on any formulation of the 3D PE, leading to alternative solutions to the traditional ADI scheme. The method developed is capable of modeling low-frequency waves interacting with irregular terrain, as well as infrasound propagating over large distances in a moving inhomogeneous media.

ACKNOWLEDGMENTS

The authors thank the two anonymous reviewers and the associate editor, Vladimir Ostashev, for their valuable suggestions that helped to improve this paper. This research was supported by AWE Blacknest. The algorithm presented above was implemented in Modern FORTRAN (2003/2008) using the LAPACK Mathematical Library (Anderson *et al.*, 1999) and the GNU Fortran compiler (version 8.x). Computations have been carried out on a sequential workstation (OSX 10.13, 16GB RAM, Intel i7). Boundary element simulations were done in COMSOL Multiphysics 5.4. The authors thank Dr. Anton Shterenlikht for his advice on scientific computing with FORTRAN.

Anderson, E., Bai, Z., Bischof, C., Blackford, L., Demmel, J., Dongarra, J., Du Croz, J., Greenbaum, A., Hammarling, S., McKenney, A., and Sorensen, D. (**1999**). *LAPACK Users' Guide* (Society for Industrial and Applied Mathematics, Philadelphia).

Attenborough, K. (**1985**). "Acoustical impedance models for outdoor ground surfaces," J. Sound Vibration **99**(4), 521–544.

Attenborough, K., Bashir, I., and Taherzadeh, S. (**2011**). "Outdoor ground impedance models," J. Acoust. Soc. Am. **129**(5), 2806–2819.

Beilis, A., and Tappert, F. D. (**1979**). "Coupled mode analysis of multiple rough surface scattering," J. Acoust. Soc. Am. **66**, 811–826.

Cheng, R., Morris, P., and Brentner, K. (**2009**). "A three dimensional parabolic equation method for sound propagation in moving inhomogeneous media," J. Acoust. Soc. Am. **126**(4), 1700–1710.

Collins, M. D. (**1989**). "A higher–order parabolic equation for wave propagation in an ocean overlying an elastic bottom," J. Acoust. Soc. Am. **86**(4), 1459–1464.

Fornberg, B. (**1988**). "Generation of finite difference formulas on arbitrarily spaced grids," Math. Comput. **51**(184), 699–706.

Godin, O. (**2002**). "An effective quiescent medium for sound propagating through an inhomogeneous, moving fluid," J. Acoust. Soc. Am. **112**(4), 1269–1275.

Jensen, F., Kuperman, W., Porter, M., and Schmidt, H. (**2011**). *Computational Ocean Acoustics*, Modern Acoustics and Signal Processing (Springer, New York).

Kampanis, N., Delis, A., Antonopoulou, D., and Kozyrakis, G. (**2013**). "A finite element discretization of the standard parabolic equation in generalized boundary fitting coordinates," Appl. Numer. Math. **67**, 152–166.

Lee, D., Botseas, G., and Siegmann, W. (**1992**). "Examination of three-dimensional effects using a propagation model with azimuth-coupling capability (FOR3D)," J. Acoust. Soc. Am. **91**(6), 3192–3202.

Lee, D., and McDaniel, S. (**1988**). "Ocean acoustic propagation by finite difference methods," *International Series in Modern Applied Mathematics and Computer Science* (Pergamon, Oxford).

Lee, D., Pierce, A., and Shang, E.-C. (**2000**). "Parabolic equation development in the twentieth century," J. Comp. Acoustics **8**(4), 527–637.

Leontovič, A. (**1944**). "On a method of solving the problem of propagation of electromagnetic waves near the surface of the earth," Izv. Akad. Nauk USSR Ser. Phys **8**, 16–22.

Lin, Y.-T. (**2019**). "Three-dimensional boundary fitted parabolic-equation model of underwater sound propagation," J. Acoust. Soc. Am. **146**(3), 2058–2067.

Lin, Y.-T., Collis, J., and Duda, T. (**2012**). "A three-dimensional parabolic equation model of sound propagation using higher-order operator splitting and Padé approximants," J. Acoust. Soc. Am. **132**(5), EL364–EL370.

Ostashev, V., and Wilson, D. (**2016**). *Acoustics in Moving Inhomogeneous Media* (CRC Press, London).

Parakkal, S., Gilbert, K., and Di, X. (**2012**). "Application of the Beilis-Tappert parabolic equation method to sound propagation over irregular terrain," J. Acoust. Soc. Am. **131**(2), 1039–1046.

Parakkal, S., Gilbert, K., Di, X., and Bass, H. (**2010**). "A generalized polar coordinate method for sound propagation over large-scale irregular terrain," J. Acoust. Soc. Am. **128**(5), 2573–2580.

Saad, Y. (**2003**). *Iterative Methods for Sparse Linear Systems* (Kluwer Academic Publisher, Dordrecht).

Sack, R., and West, M. (**1995**). "A parabolic equation for sound propagation in two dimensions over any smooth terrain profile: The generalized terrain parabolic equation (GT-PE)," Applied Acoustics **45**, 113–129.

Salomons, E. (**2001**). *Computational Atmospheric Acoustics* (Kluwer Academic Publisher, Dordrecht).

Siegmann, W., Kriegsmann, G., and Lee, D. (**1985**). "A wide-angle three-dimensional parabolic wave equation," J. Acoust. Soc. Am. **78**(2), 659–664.

Silva, M., Costa, E., and Liniger, M. (**2012**). "Analysis of the effects of irregular terrain on radio wave propagation based on a three-dimensional parabolic equation," IEEE Trans. Antenna Propag. **60**(4), 2138–2143.

Simoncini, V. (**2016**). "Computational methods for linear matrix equations," SIAM Rev. **58**(3), 377–441.

Sturm, F. (**2005**). "Numerical study of broadband sound pulse propagation in three-dimensional oceanic waveguides," J. Acoust. Soc. Am. **117**(3), 1058–1079.

Sturm, F., and Kampanis, N. (**2007**). "Accurate treatment of a general sloping interface in a finite-element 3D narrow-angle PE model," J. Comp. Acoustics **15**(3), 285–318.

Tappert, F. (**1977**). "The parabolic approximation method," in *Wave Propagation and Underwater Acoustics* (Springer, Berlin Heidelberg), 224–287.

Thomson, D. J., and Chapman, N. R. (**1983**). "A wide–angle split–step algorithm for the parabolic equation," J. Acoust. Soc. Am. **74**(6), 1848–1854.

Van Loan, C. F., and Golub, G. H. (**1983**). *Matrix Computations* (Johns Hopkins University Press, Baltimore).

West, M., Gilbert, K., and Sack, R. (**1992**). "A tutorial on the parabolic equation (PE) model used for long range sound propagation in the atmosphere," Appl. Acoust. **37**(1), 31–49.

White, M. (**1989**). "Application of the parabolic equation to the outdoor propagation of sound," Appl. Acoust. **27**(3), 227–238.

Xie, L., Ding, J., and Ding, F. (**2009**). "Gradient based iterative solutions for general linear matrix equations," Comput. Math. Appl. **58**(7), 1441–1448.

Xu, C.-X., Tang, J., Piao, S.-C., Liu, J.-Q., and Zhang, S.-Z. (**2016**). "Developments of parabolic equation method in the period of 2000–2016," Chinese Phys. B **25**, 124315.

Zelley, C., and Constantinou, C. (**1999**). "A three-dimensional parabolic equation applied to VHF/UHF propagation over irregular terrain," IEEE Trans. Antenna Propag. **47**(10), 1586–1596.

Zhu, D., and Bjørnø, L. (**2000**). "A three-dimensional, two-way, parabolic equation model for acoustic backscattering in a cylindrical coordinate system," J. Acoust. Soc. Am. **108**(3), 889–898.